THE FLOW FIELD INSIDE A RANQUE-HILSCH VORTEX TUBE PART I: EXPERIMENTAL ANALYSIS USING PLANAR FILTERED RAYLEIGH SCATTERING

Ulrich Doll, Eike Burow, Manfred Beversdorff, Guido Stockhausen, Christian Willert
Department of Engine Measurement Systems
Institute of Propulsion Technology, German Aerospace Center (DLR)
Linder Hoehe, 51147 Cologne, Germany
ulrich.doll@dlr.de

Christian Morsbach[1], Daniel Schlüß[1], Martin Franke[2]
Department of Numerical Methods
Institute of Propulsion Technology, German Aerospace Center (DLR)
[1]Linder Hoehe, 51147 Cologne, Germany; [2]Mueller-Breslau-Str. 8, 10623 Berlin, Germany

ABSTRACT

The flow field of a Ranque-Hilsch vortex tube is characterized experimentally. Firstly conventional probe based technology is used in order to measure inlet and outlet temperatures as well as to acquire temporally resolved wall pressure data over a wide range of operating conditions. Secondly the filtered Rayleigh scattering technique is employed in order to gather detailed temporally averaged planar information on the vortex tube's flow topology. These measurements form the basis of a detailed numerical study in part II of this contribution.

INTRODUCTION

The effect, that pressurized air, injected into a cylindrical tube is cooled down at one end and heated up at the other was first discovered by Ranque (1933) and then investigated and improved by Hilsch (1947). Since it's invention the Ranque-Hilsch vortex tube (RHVT) has found a variety of industrial applications, including spot cooling of electronic controls as well as gas dehydration or condensate removal.

This contribution is the first part of a joint effort of the Institute of Propulsion Technology's Engine Measurement Systems and Numerical Methods departments. Part I will focus on an experimental characterization of the RHVT's flow field in terms of pressure, temperature and velocity. Part II (Morsbach *et al.*, 2015) will contain a detailed numerical analysis of the vortex tube based on unsteady RANS methods. In order to account for the complex nature of the RHVT's flow field, the device will be simulated using turbulence models of increasing complexity. Numerical and experimental results will then be compared in detail.

The underlying mechanisms of the temperature separation process inside the RHVT are still controversially discussed in the literature. In their review article, Eiamsa-ard & Promvonge (2008) give a detailed overview on the different hypotheses used to explain the energy separation effect, including adiabatic expansion, internal friction, static temperature gradients and acoustic streaming. In Xue *et al.* (2010), present theories are summarized and subjected to a critical review. The authors point out that, due to the high complexity of the RHVT's flow field, several studies found in the literature come to contradictory conclusions. In this respect, the authors aim at the identification of existing knowledge gaps.

In Xue *et al.* (2013, 2014), the authors develop a theory regarding the temperature separation process in a counterflow type vortex tube. When pressurized air is injected tangentially into the tube, a vortex is formed in the peripheral region, which travels in axial direction towards the hot exit. Part of the air near the tube's axis turns around and streams back towards the cold exit. As the flow expands from a high to a low pressure region, this process leads to a temperature drop in the tube's center. While most of the peripheral flow exits the tube directly through the hot exit, parts of it are forced back and enter a multi-circulation flow pattern, which is claimed to be responsible for the temperature rise at the hot end, when interacting (by partial stagnation and mixture) with the peripheral flow. The cold core at the front and the hot region at the rear part are divided by a separating region. It prevents hot and cold areas from mixing and is deemed important for tube performance. Based on the heat pump assumption made by Ahlborn & Gordon (2000), Liew *et al.* (2012*b*) use a different approach to explain the temperature separation process. Due to centrifugal forces, a radial pressure gradient exists inside the tube. On the one hand, if gas is moved towards the wall in radial direction, it will be compressed adiabatically and heats up consequently. On the other hand, if gas is moved from the periphery towards the tube's center, it expands and cools down. This process can only be maintained if radial velocity fluctuations, mainly due to turbulent mixing, are present. Instead of a single heat pump driven by a secondary circulation (Ahlborn & Gordon, 2000), a system of turbulent eddies causes a transfer of heat from the inside to the outside. Such a flow pattern was also identified in a numerical study by Secchiaroli *et al.* (2009). An alternative approach is fol-

lowed by Kurosaka (1982). He claims acoustic streaming, induced by orderly, periodic disturbances, to be responsible for the temperature separation process. By distorting the time-averaged flow field, these acoustic perturbations force the initial Rankine-vortex into a forced vortex structure. At the same time, a radial gradient in total temperature emerges. To support his theory, Kurosaka modified an uniflow type vortex tube with an additional acoustic cavity and measured the frequency content as well as the temperature at the tube's centerline. The spectral analysis revealed a fundamental frequency accompanied by it's higher harmonics. In increasing the tube's inlet pressure, the fundamental frequency was growing accordingly. When the acoustic cavity's resonance was reached, the sound pressure level (SPL) of the fundamental frequency suddenly dropped by 25 dB, accompanied with a rise of 35 °C in temperature.

In order to get insight into the complex three dimensional flow topology and to confirm or abandon existing theories describing the temperature separation inside the tube, information on the relevant flow quantities pressure, temperature and velocity are needed (Gao *et al.*, 2005). Most experimental studies rely on conventional probe based technology, namely Pitot probes or similar devices and thermocouples, which are introduced into the flow field at distinct axial positions and traversed radially from the tube's central axis towards the wall (see e. g. Ahlborn & Gordon (2000); Gao *et al.* (2005); Xue *et al.* (2013)). Despite their high temporal resolution, these devices measure point-wise only and, additionally, have a strong blocking impact on the flow field (3 to 26 % of the tube's cross sectional area (Gao *et al.*, 2005)). In this respect, optical measurement techniques offer a viable opportunity, as a key attribute of these techniques is their minimal-invasive nature. In Liew *et al.* (2012*a*), a PDPA[1] system was used to infer three-component velocities and sizes of water droplets added to the flow. They found a low signal to noise ratio caused by high fluctuation intensities in the tube's core region. Similar observations were made in velocity measurements using L2F[2] in Doll *et al.* (2014*a*), were the seeding density near the tube's center was not sufficient to acquire reliable data. This stresses the fact, that, due to high centrifugal acceleration, optical techniques relying on tracer particles have limitations in providing accurate information on the flow field inside a RHVT (Secchiaroli *et al.*, 2009). In this respect, the filtered Rayleigh scattering (FRS) technique (Miles & Lempert, 1990), extended by the method of frequency scanning (Forkey *et al.*, 1996; Doll *et al.*, 2014*b*) was chosen, as it is able to provide time averaged planar information on pressure, temperature and velocity through the Doppler shift simultaneously. The method relies on elastic molecular scattering only and thus is not susceptible to unwanted tracer particle effects.

The experimental investigation of the vortex tube will be twofold. The first part will focus on a global characterization of the device's output temperatures over a wide range of operating conditions. While running the vortex tube, a whistling tone can be recognized. In consequence it was decided to measure the wall pressure at different axial positions in parallel and to analyze it's frequency content. The findings of the first part will be used to determine an operating condition of interest, which will be subjected to a detailed characterization by optical measurements as well as numerical methods in the second part of this contribution.

[1] phase Doppler particle analysis
[2] Laser-2-Focus

EXPERIMENTAL CONFIGURATION

Vortex tube and global characterization

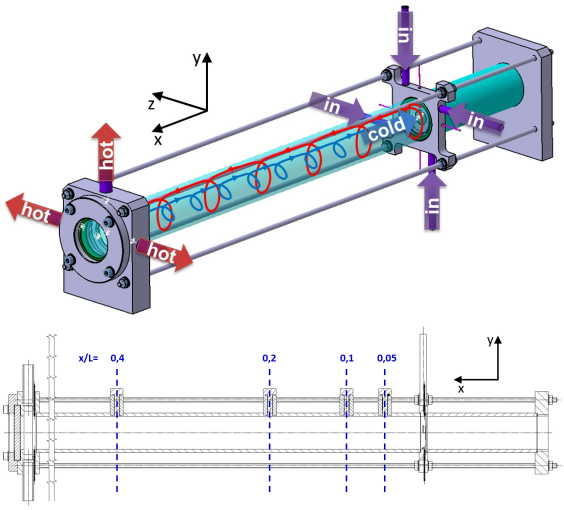

Figure 1. (*top*) Pressurized air is blown tangentially into the vortex chamber from four sides. The heated air stream exits the tube through three channels on the left (hot exit), cooled air flows through an orifice on the right (cold exit). (*bottom*) Axial positions of wall pressure measurements.

A 3D sketch of the RHVT investigated in this study is shown in Fig. 1 (*top*). The device consists of a cylindrical tube of 700 mm in length and 30 mm in diameter, made of quartz glass, in order to provide optical accessibility throughout the tube's length. The flow field inside the vortex tube can be characterized by the cold fraction $\varepsilon = \dot{m}_{cold}/\dot{m}$, being the mass flow ratio of cold air to total air flow (Hilsch, 1947). The ratio can be regulated by a valve downstream from the hot exit. Temperatures T_0 at the inlet, T_h at the hot and T_c at the cold exit are monitored by Pt-100 resistance thermometers at a rate of 2 Hz. A metal version of the vortex tube was constructed in order to allow for wall pressure measurements. Fig. 1 (*bottom*) shows a sectional view of the metal tube. The original design was modified by four bores at $x/L = 0.05$, 0.1, 0.2 and 0.4. At each position, the wall pressure was measured by means of a Kulite piezoelectric sensor at a rate of 50 kHz.

Hilsch (1947) identifies a multitude of attributes, which have substantial influence on the temperature separation effect. The list includes geometric properties such as length and diameter of the tube, geometry and number of inlet nozzles as well as the orifice diameter at the cold exit, temperature and pressure of the inflowing air and the above mentioned cold fraction. In this respect, as all geometric properties remained unchanged and the inlet parameters were held constant, the global characterization was limited to a variation of the cold fraction. For air with an absolute pressure of $p_0 = 7$ bar at $T_0 = 294$ K, resulting in a total mass flow of 11 g/s distributed to four entry nozzles, ε was varied between 0.2 and 0.65 in 0.05 steps. For each operating condition, temperatures at the inlet, hot and cold exit as well as the wall pressure at each axial position were recorded for 60 s.

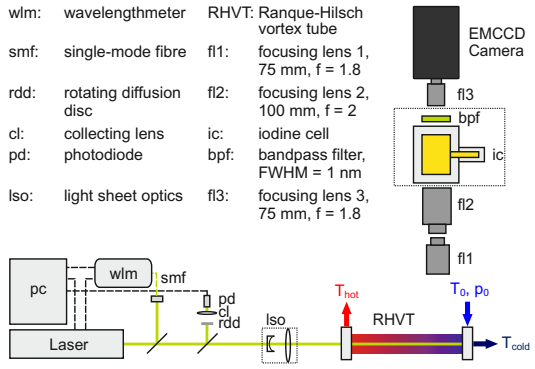

Figure 2. FRS setup

FRS measurements

Fig. 2 gives an overview of the FRS measurement's setup. The system is based on a Coherent Verdi V5 continuous wave diode-pumped solid state frequency-doubled Nd: YVO_4 laser. The laser emits single-frequency light at 532 nm with a bandwidth below 5 MHz and an adjustable output power of up to 5 W. The laser system features three options to alter its output frequency: a heated intra-cavity etalon can be used for large frequency modifications, while, by issuing control voltages onto two piezoelectric elements, the resonator's length can be modified. The laser's output frequency is monitored and controlled by a High Finesse WSU 10 wavelength meter. The device has an absolute accuracy of 10 MHz. A built-in PID controller is used to stabilize the frequency within 2 MHz of a given setpoint. A second control loop accounts for thermal effects in the laser's resonator and ensures long-term frequency stability.

As the FRS signal has to be normalized to the laser's output power, a small amount of laser light is deflected from the main beam and directed onto a rotating diffusion disk. Behind the disk, a structureless and homogeneous intensity distribution is produced. Light scattered from the disk is then collected by a lens and focused onto a photodiode. Thus the laser's output power can be measured with a relative accuracy below 0.5 %.

The laser is formed into a light sheet of ∼30 mm height and varying thickness (from 0.6 mm at cold exit to 2 mm at hot exit) using an optical scanner arrangement specifically designed for long camera exposures (Roehle & Willert, 2001) and enters the vortex tube through a flat window at the hot exit. The detector is oriented perpendicular to propagation and polarization of the laser to maximize the Rayleigh scattering's intensity (Miles *et al.*, 2001). The scattered radiation is collected by a first focusing lens and enters the transfer optics, which is composed of two additional focusing lenses in retro position. In between, the molecular iodine filter cell as well as a bandpass filter (FWHM 1 nm) are placed. Light exiting the filter array is then collected by a Hamamatsu C9100-13 EM-CCD camera. With a field of view of 53.5 x 53.5 mm^2 and the camera driven with a 2 x 2 hardware binning, this resulted in a resolution of 0.21 mm per pixel element. In order to cover the whole length of the vortex tube, the detector unit was traversed 14 times successively in axial direction. In frequency scanning FRS, the laser's output frequency is shifted multiple times along the molecular filter's transmission curve. This results in intensity spectra for each camera pixel element, from which the flow quantities pressure, temperature and Doppler shift (velocity) can be deduced. In this study, a data set for each of the 14 measurement planes was produced. The laser was tuned 32 times with an increment of ∼ 60 MHz in frequency and light was accumulated for 6 s per frequency step. The resulting intensity spectra are averaged from three consecutive measurements, leading to a total test period of ∼ 20 minutes per measurement plane.

When operating the vortex tube, large refractive index variations, mainly near the tube axis, cause a redistribution of the light sheet's intensity. As described in Doll *et al.* (2014*a*), the data cannot be evaluated by the standard procedure, but a normalization approach must be used. By normalizing the data, a significant amount of the measurement signal's sensitivity to pressure is lost, with uncertainties rising up to 7 %. Thus, pressure results will not be presented. Still, the data can be used to extract high quality information on temperature and velocity, with uncertainties below 2 %.

Results

ε-Variation

In Fig. 3, temperatures at the hot and the cold exit as well as the temperature difference $T_h - T_c$ between both exits are plotted against the cold fraction ε. At $\varepsilon = 0.2$, temperatures at both exits reach a minimum, with $T_h - T_c =$ 22.5 K. With increasing cold fraction, T_h and T_c grow steadily, with a stronger gain in temperature toward the hot exit. Following the cold fraction at $\varepsilon = 0.55$, this tendency is further intensified. When arriving at the largest cold fraction at 0.65, the temperature difference between hot and cold exit totals ∼33 K.

Fig. 4 shows amplitude spectra extracted from the wall pressure measurements for cold fractions of $\varepsilon = 0.2$ (*top*) and 0.3 (*bottom*) at the four axial positions. Based on this analysis, the above mentioned whistling tone can be assigned to a structure comprised of several distinct peaks, with frequency values ranging from 12.1 to 12.9 kHz. Compared to $\varepsilon = 0.3$, for a cold fraction of 0.2, the structure is less pronounced and is further attenuated with increasing x/L. While all amplitude spectra at $x/L = 0.05$ and 0.1 exhibit almost no frequency shares below 10 kHz, at $x/L = 0.2$, accompanied with the amplitudes of the whistling tone's frequencies going down, five broadband

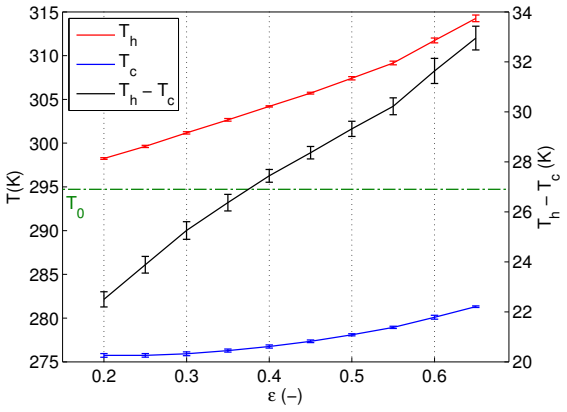

Figure 3. Characteristic curves: (*top*) Averaged temperatures T_h (red) at hot exit, T_c (blue) at cold exit and temperature difference $T_h - T_c$ (black) plotted against ε

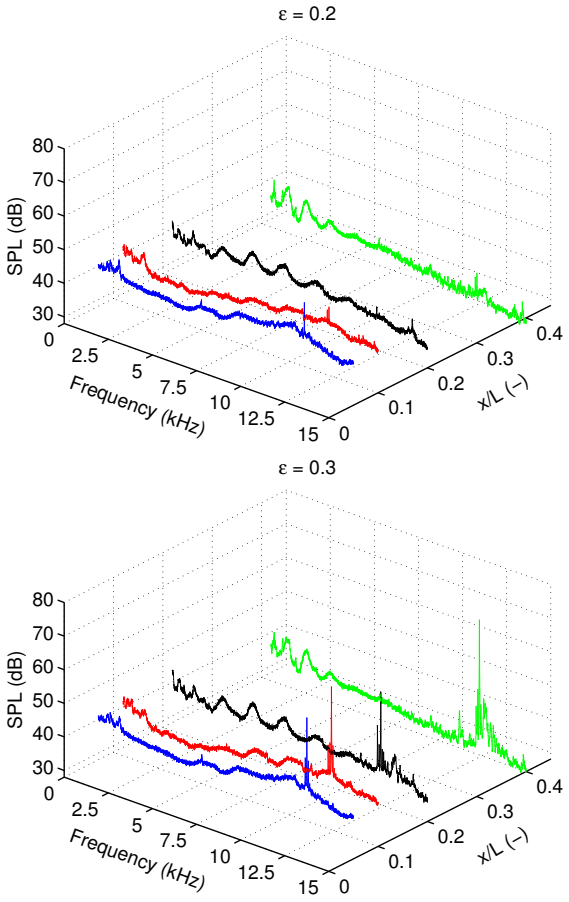

Figure 4. Frequency analysis of wall pressure: Amplitude spectra for $\varepsilon = 0.2$ (*top*) and $\varepsilon = 0.3$ (*bottom*) at $x/L = 0.05$ (blue), 0.1 (red), 0.2 (black) and 0.4 (green).

structures emerge, with central frequencies at 3.42, 5.1, 6.87, 8.77 and 10.58 kHz. When reaching the last axial position at $x/L = 0.4$, the five broadband frequency structures disappear.

The vortex tube's global characterization through a variation of the cold fraction ε revealed several interesting aspects. While the characteristic temperature curve of Fig. 3 (*top*) is in good qualitative agreement to previous studies (Ahlborn & Gordon, 2000; Liew *et al.*, 2012*a*), a fundamental frequency, associated with the swirl velocity of the main vortex, accompanied by it's higher harmonics as reported in Kurosaka (1982), Gao (2005) and Liew *et al.* (2012*a*) is not noticeable in the spectral analysis of the wall pressure data for $x/L = 0.05$, 0.1 or 0.4. Only at an axial position of $x/L = 0.2$ a regular formation of broadband structures emerges, which bears resemblance to a frequency pattern comprised of several harmonic orders. From the distance between two consecutive peaks, it's fundamental frequency f_0 can be estimated to lie between 1.7 to 1.9 kHz. The fact, that the whistling tone's amplitude from $x/L = 0.1$ to 0.2 is decreased accompanied with five broadband frequency structures emerging, then from $x/L = 0.2$ to 0.4 again rises to it's original level with the low frequency pattern vanishing, suggests a coupling between flow field and acoustics. Based on these findings, a cold fraction of $\varepsilon = 0.3$ was chosen for the detailed experimental and numerical investigations. At this operating condition, on the one hand, the spectral characteristics identified above are fully developed and on the other hand, the amplitudes of the whistling tone's frequencies are at maximum.

FRS results

In this section, temperature as well as velocity results will be presented. The optical Doppler shift $\Delta\nu$ is defined as

$$\Delta\nu = \nu - \nu_0 = \frac{\nu_0}{c}(\mathbf{o} - \mathbf{l}) \cdot \mathbf{u}, \qquad (1)$$

with ν_0 being the excitation frequency, ν the frequency of the scattered light, c the speed of light, $\mathbf{o}$ the unit vector, pointing from the scattering volume to the observer, $\mathbf{l}$ the unit vector in direction of the laser's propagation and $\mathbf{u}$ the three-component velocity vector. Thus, $\Delta\nu$ is proportional to the projection of the velocity vector onto the bisector spanned by $\mathbf{o}$ and $\mathbf{l}$. In order to measure all three components U_x, U_y and U_z of the velocity vector $\mathbf{u}$, two additional Doppler shift values would be needed.

Due to the optical arrangement, there is virtually no sensitivity to the radial velocity component U_y. Additionally, it is reasonable to assume the flow field to be rotationally symmetric with respect to the tube axis. With $\mathbf{l} = (-1, 0, 0)$ and $\mathbf{o} = (o_x, o_y, o_z)$, axial and circumferential velocity components can be calculated from

$$U_x = \frac{c(\Delta\nu(y) + \Delta\nu(-y))}{2\nu_0(o_x - 1)}, \; U_z = \frac{c(\Delta\nu(y) - \Delta\nu(-y))}{2\nu_0 o_z} \qquad (2)$$

for each camera pixel element.

Fig. 5 gives an overview of resulting temperature T (*top*), axial velocity U_x (*middle*) and circumferential velocity U_z (*bottom*) maps, covering the full height and length of the vortex tube's central x-y-plane. Apparently, temperature as well as velocity maps exhibit discontinuities at the intersection between two successive measurement planes. The cause is believed to be related to an insufficient stability of the set operating condition. Furthermore, the white coloured regions mark areas of heightened residuals from the data fitting procedure, where results are less reliable.

The temperature map of Fig. 5 (*top*) exhibits the lowest temperatures in the upper and lower left corners, where absolute values near 240 K are reached. In these regions, the transonic tangential air injection governs the flow field. The first third of the vortex tube's temperature field exhibits an almost conical structure, extending to an x/L around 0.3. On the tube's centerline, temperature values rise from 270 K near the cold exit to reach the inlet temperature of 294 K at the cone's vertex. In the following, the temperature gradually grows towards the hot exit, reaching maximum values of around 310 K in the upper and lower right corners. Despite a declining temperature difference between central region and periphery, a colder core at the tube axis persists as far as the hot exit.

In Fig. 5 (*middle*), the distribution of the axial velocity component U_x is plotted in false colours. In vertical direction, the map can be divided into two main regions: a peripheral and a core area. Beginning at the tangential air injection where the highest absolute values in axial velocity are reached, the peripheral area ends opposite at the hot exit with velocities gradually falling throughout the tube. Near the injection, the region is less developed, extending barely

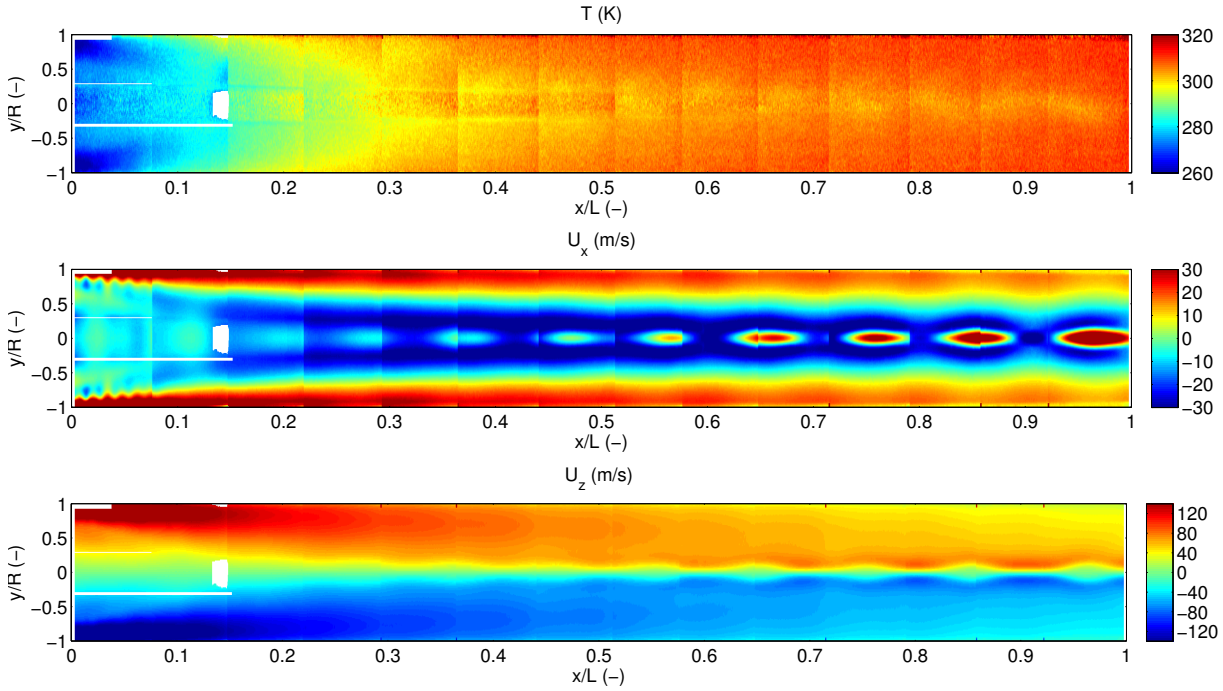

Figure 5. Temperature (*top*), axial (*middle*) and circumferential velocity (*bottom*) maps, comprised of 14 consecutive measurement positions.

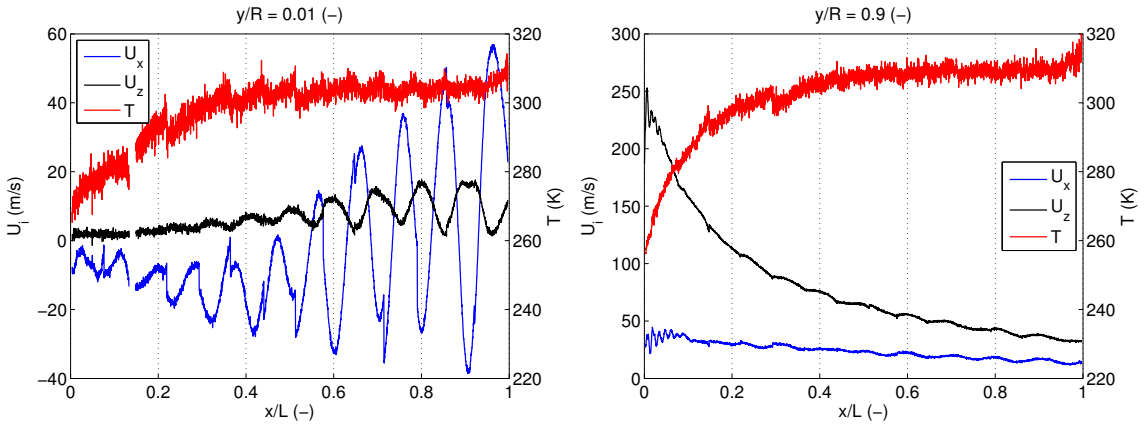

Figure 6. Profiles of U_x (blue), U_z (black) and T (red) for $y/R = 0.01$ (*top*) and y/R=0.9 (*bottom*).

2 mm from the wall, exhibiting a short-wave wave structure. Developing further downstream, the short-wave structure is smoothed and changes into a long-wave form, till it reaches it's full extent of $\sim$ 6.25 mm. While moving further vertically towards the tube's axis, velocities approach zero and, after a sign change, the air streams back in the opposite direction towards the cold exit. According to the peripheral flow being less pronounced at the tube's front, the lager part of the area is occupied by the core region. It's extent reduces gradually when moving further downstream towards the hot exit, until peripheral and core flow claim an almost similar portion of the tube's cross section. What immediately attracts attention while examining the axial velocity distribution is a regular flow pattern emerging at the tube axis. Right from the start distinct zones can be recognized, where absolute values of axial velocity differ from the surrounding fluid. Whereas in the tube's front section up to $x/L = 0.3$ these zones appear somewhat washed out, their ellipsoidal shape becomes more and more distinguishable with growing axial distance. While in the tube's front half, velocities within these formations as well as of the surrounding flow remain negative, in the rear, air moving back from the hot towards the cold exit encloses kernels of positive axial velocity, whose amplitudes partially exceed those of the surrounding flow.

The distribution of the circumferential velocity component U_z in Fig. 5 (*bottom*) is dominated by the swirl of the main vortex. Absolute values reach their maximum near the tangential air injection and gradually decrease with growing axial distance. Despite the dominating swirl, the regular flow pattern in the tube's core region is clearly recognizable, on the one hand by expanding the low velocity region around the tube axis, on the other hand by imposing a wave like structure onto the circumferential velocity field.

In Fig. 6, axial profiles of U_x, U_z and T at $y/R = 0.01$ (*top*) near the tube's axis and at $y/R = 0.9$ (*bottom*) are plotted against x/L. In Fig. 6 (*top*), U_x as well as U_z velocity curves bear reminiscence to a driven oscillation, with

growing amplitudes towards the hot exit. As indicated in the previous paragraph, the bulk temperature increase happens until $x/L = 0.3$. Up to $x/L = 0.9$ there is only a slight growth, intensifying again towards the hot exit. In Fig. 6 (*bottom*), U_z exhibits the strongest dynamics with velocities exceeding 250 m/s in the vicinity of the tangential air injection, falling steeply below 90 m/s after one third of the tube's length already. Due to the influence of the expansion, both velocity components present rather chaotic flow patterns up to $x/L = 0.1$, becoming smoother towards the hot exit. Nevertheless, the oscillating structure of U_x and U_z, which is predominant near the tube's axis, still prevails in the periphery. The temperature curves of Fig. 6 (*top*) and (*bottom*) show similar characteristics, with absolute values growing slightly faster at $y/R = 0.9$. Behind $x/L = 0.15$, temperatures at the tube's periphery lie ~ 5 K above correspondent values at the axis.

Whereas the circumferential velocity in Fig. 6 (*top*) seems to be nearly unaffected by the slight instability of the operating point, axial component as well as temperature curve are biased by discontinuities. For instance at $x/L = 0.22$, U_x jumps by 8.8 m/s from -7.5 to -16.3 m/s, resulting in a sudden drop from 295 to 291.5 K in temperature. This, on the one hand unwanted effect of system instability, points to a strong relationship between axial velocity and heat release on the other.

CONCLUSION

The flow field within a Ranque-Hilsch vortex tube was characterized by varying the cold fraction parameter ε over a wide range and measuring inlet and outlet temperatures as well as wall pressure at distinct axial positions. Based on these measurements, a cold fraction of 0.3 was chosen for a detailed analysis of the vortex tube's temporally averaged flow topology using the filtered Rayleigh scattering technique. Spatially highly resolved results of the RHVT's temperature, axial and circumferential velocity fields were obtained, covering the devices total height and length. According to Kurosaka (1982), acoustic streaming, the distortion of the time-averaged flow field by high amplitude acoustic perturbations, is one of the main mechanisms behind the temperature separation. In conclusion, the findings of this contribution suggest a strong relationship between acoustic phenomena and the time-averaged flow field.

REFERENCES

Ahlborn, Boye K. & Gordon, Jeffrey M. 2000 The vortex tube as a classic thermodynamic refrigeration cycle. *Journal of Applied Physics* **88** (6), 3645–3653.

Doll, Ulrich, Beversdorff, Manfred, Stockhausen, Guido, Willert, Christian, Schlüß, Daniel & Morsbach, Christian 2014*a* Characterization of the flow field inside a ranque-hilsch vortex tube using filtered rayleigh scattering, laser-2-focus velocimetry and numerical methods. In *17th Int Symp on Applications of Laser Techniques to Fluid Mechanics*. Lisbon, Portugal.

Doll, Ulrich, Stockhausen, Guido & Willert, Christian 2014*b* Endoscopic filtered rayleigh scattering for the analysis of ducted gas flows. *Experiments in Fluids* **55** (3), 1–13.

Eiamsa-ard & Promvonge 2008 Review of ranque-hilsch effects in vortex tubes. *Renewable and Sustainable Energy Reviews* **12** (7), 1822 – 1842.

Forkey, JN, Finkelstein, ND, Lempert, WR & Miles, RB 1996 Demonstration and characterization of filtered rayleigh scattering for planar velocity measurements: Aerodynamic measurement technology. *AIAA journal* **34** (3), 442–448.

Gao, Chengming 2005 Experimental study on the ranque-hilsch vortex tube. PhD thesis, Technische Universiteit Eindhoven.

Gao, C.M., Bosschaart, K.J., Zeegers, J.C.H. & de Waele, A.T.A.M. 2005 Experimental study on a simple ranque-hilsch vortex tube. *Cryogenics* **45** (3), 173 – 183.

Hilsch, R. 1947 The use of the expansion of gases in a centrifugal field as cooling process. *Review of Scientific Instruments* **18** (2), 108–113.

Kurosaka, M. 1982 Acoustic streaming in swirling flow and the ranque-hilsch (vortex-tube) effect. *Journal of Fluid Mechanics* **124**, 139–172.

Liew, R., Zeegers, J.C.H., Kuerten, J.G.M. & Michalek, W. R. 2012*a* 3d velocimetry and droplet sizing in the ranque-hilsch vortex tube. *Experiments in Fluids* **54** (1).

Liew, R., Zeegers, J. C. H., Kuerten, J. G. M. & Michalek, W. R. 2012*b* Maxwell's demon in the ranque-hilsch vortex tube. *Phys. Rev. Lett.* **109**, 054503.

Miles, R. & Lempert, W. 1990 Two-dimensional measurement of density, velocity, and temperature in turbulent high-speed air flows by uv rayleigh scattering. *Applied Physics B: Lasers and Optics* **51**, 1–7, 10.1007/BF00332317.

Miles, Richard B, Lempert, Walter R & Forkey, Joseph N 2001 Laser Rayleigh scattering. *Measurement Science and Technology* **12** (5), R33.

Morsbach, Christian, Schlüß, Daniel, Franke, Martin, Doll, Ulrich, Burow, Eike, Beversdorff, Manfred, Stockhausen, Guido & Willert, Christian 2015 The flow field inside a Ranque-Hilsch vortex tube part II: Turbulence modelling and numerical simulation. In *Ninth International Symposium on Turbulence Shear Flow Phenomena (TSFP-9)*. Melbourne, Australia.

Ranque, G. J. 1933 Expériences sur la détente giratoire avec productions simultanées d'un echappement d'air chaud et d'un echappement d'air froid. *Journal de Physique et Le Radium* **4** (7), 112–114.

Roehle, I & Willert, C E 2001 Extension of Doppler global velocimetry to periodic flows. *Measurement Science and Technology* **12** (4), 420.

Secchiaroli, A., Ricci, R., Montelpare, S. & D'Alessandro, V. 2009 Numerical simulation of turbulent flow in a ranque-hilsch vortex tube. *International Journal of Heat and Mass Transfer* **52** (23-24), 5496–5511, cited By (since 1996)22.

Xue, Y., Arjomandi, M. & Kelso, R. 2010 A critical review of temperature separation in a vortex tube. *Experimental Thermal and Fluid Science* **34** (8), 1367–1374.

Xue, Y., Arjomandi, M. & Kelso, R. 2013 The working principle of a vortex tube. *International Journal of Refrigeration* **36** (6), 1730 – 1740.

Xue, Y., Arjomandi, M. & Kelso, R. 2014 Energy analysis within a vortex tube. *Experimental Thermal and Fluid Science* **52** (0), 139 – 145.